EES Solar

PAPER

View Article Online
View Journal

Cite this: DOI: 10.1039/d5el00192g

Bias-free, high-rate solar hydrogen production in alkaline media with a NiCo-coupled perovskite photocathode

Minseo Lee,† Wooyeon Kim,† Hayoung Kim,† Seoyeong Lee, Min Jae Ko* and Youn Jeong Jang*

Photoelectrochemical (PEC) water splitting provides a sustainable route for hydrogen production from solar energy. In this work, we demonstrate a bias-free PEC cell integrating a perovskite photocathode with a bifunctional NiCo electrocatalyst and pairing it with a NiCo-coated Ni foam anode. To minimize anodic overpotential, the oxygen evolution reaction (OER) is replaced with the hydrazine oxidation reaction (HzOR, $E° = -0.33$ V_{RHE}), enabling efficient operation under alkaline conditions. This architecture achieves a photocurrent density of -24 mA cm^{-2} with a photovoltage of 0.99 V under AM 1.5G illumination, among the highest reported for a bias-free PEC cell. Beyond solar-to-hydrogen conversion, this system simultaneously detoxifies hydrazine, establishing a dual-functional platform for sustainable fuel production and environmental remediation. These findings highlight the practical potential of integrating high-performance perovskite photoelectrodes with alternative anodic reactions to overcome efficiency and stability barriers in solar-to-hydrogen conversion.

Received 18th November 2025
Accepted 5th May 2026

DOI: 10.1039/d5el00192g

rsc.li/EESSolar

Broader context

Hydrogen is a key carbon-free energy carrier for future sustainable energy systems. Among various production routes, photoelectrochemical (PEC) water splitting is particularly attractive, as it enables direct solar-to-hydrogen conversion. For practical application, bias-free operation—without external electrical input—is highly desirable. However, water electrolysis has been predominantly performed in acidic media, where precious-metal catalysts such as Pt are typically required, leading to high cost and corrosion-induced instability. In contrast, alkaline water electrolysis allows the use of earth-abundant transition metals like Ni and Co with higher stability, yet their performance has generally been lower than acidic systems. Despite these challenges, we demonstrate a bias-free PEC system in alkaline media that achieves the highest hydrogen production rate reported to date. The device employs a perovskite photocathode integrated with a NiCo catalyst and NiCo-coated Ni foam anode. Notably, hydrazine oxidation is utilized as the anodic reaction, which significantly lowers the potential requirement.

1. Introduction

Hydrogen (H_2) is a promising carbon-free energy carrier owing to its high gravimetric energy density (141.9 MJ kg^{-1}), offering a viable pathway toward sustainable energy systems.[1–3] Water splitting provides a direct route for green hydrogen generation using renewable energy sources without carbon emissions. In particular, acidic electrolytes are often employed because they enable efficient proton transport and high catalytic activity of noble metal catalysts such as platinum (Pt) and iridium (Ir). However, their practical application is limited by the high cost and scarcity of noble metals, as well as corrosion-induced instability under acidic conditions.[4–8] Furthermore, the oxygen evolution reaction (OER; $2H_2O \rightarrow O_2 + 4H^+ + 4e^-$) in acidic media requires a large anodic overpotential, severely limiting overall energy efficiency.

In contrast, alkaline water electrolysis is an attractive alternative because it enables the use of non-precious, earth-abundant transition metals such as nickel (Ni), cobalt (Co), and iron (Fe), which exhibit improved stability and durability under alkaline conditions.[9–11] Ni-based catalysts are particularly effective for the hydrogen evolution reaction (HER; $H_2O + 2e^- \rightarrow H_2 + 2OH^-$), benefiting from their high conductivity and chemical robustness. Incorporation of Co further enhances HER activity by accelerating water dissociation and interfacial charge transfer, resulting in well-documented synergistic effects in a NiCo bimetallic catalyst.[12,13]

While alkaline water electrolysis mitigates cost and stability concerns, achieving sufficient driving potential remains a challenge. Photoelectrochemical (PEC) water splitting has therefore emerged as an attractive strategy for direct solar-to-chemical energy conversion, in which semiconductor absorbers

Department of Chemical Engineering, Hanyang University, 222, Wangsimni-ro, Seongdong-gu, Seoul, 04763, Republic of Korea. E-mail: mjko@hanyang.ac.kr; yjang53@hanyang.ac.kr

† These authors contributed equally: Minseo Lee, Wooyeon Kim and Hayoung Kim.

generate photovoltage to drive overall water splitting.[14,15] Lead halide perovskites (PVKs) have recently been highlighted as promising photocathodes due to their optimal band gap (~1.6 eV), high absorption coefficient, and excellent carrier transport properties, enabling efficient PEC operation without requiring tandem architectures.[16,17] However, even in PEC systems, the sluggish OER kinetics impose substantial energy losses and constrain system efficiency.

To overcome this challenge, alternative anodic reactions such as the urea oxidation reaction (UOR), alcohol oxidation reaction (AOR), and hydrazine (N_2H_4) oxidation reaction (HzOR) have been investigated.[18,19] Among these, the HzOR (N_2H_4 + $4OH^- \rightarrow N_2 + 4H_2O + 4e^-$, $E^\circ = -0.33$ V_{RHE}) is particularly advantageous, requiring the lowest thermodynamic potential while simultaneously detoxifying hazardous N_2H_4 into benign nitrogen (N_2). Moreover, it serves as a useful proof-of-concept anodic reaction, highlighting dual benefits in energy efficiency and environmental remediation.[20]

Here, we demonstrate a bias-free PEC cell composed of a PVK photocathode integrated with a bifunctional NiCo catalyst and paired with a NiCo-coated Ni foam (NF) anode. By replacing the OER with the HzOR, the anodic potential requirement is significantly reduced, enabling efficient bias-free operation under alkaline conditions. The PVK/NiCo photocathode delivers a high photocurrent density of −24 mA cm^{-2} with a photovoltage of 0.99 V under AM 1.5G illumination, achieving stable hydrogen generation without tandem architecture. In addition, simultaneous hydrazine degradation enhances the practical value of this PEC platform, establishing a dual-functional system for sustainable solar fuel production and environmental protection.

2. Results and discussion

2.1. Design of unbiased solar hydrogen production

Solar-driven hydrogen production utilizes a dual-component cell that integrates PEC hydrogen production with the HzOR (Fig. 1a). The photocathode, composed of a light-absorbing PVK integrated with a NiCo electrocatalyst, facilitates the HER. The anode, featuring NiCo-deposited NF, functions as a catalyst for the HzOR. To ensure stability and water resistance, the PVK photocathode was encapsulated by NiCo using field's metal (FM) and titanium (Ti) foil, with epoxy sealing the edges. Under illumination, photogenerated charge carriers are separated within the PVK absorber; electrons are transported to the NiCo catalytic surface *via* the FM/Ti foil composite, while photogenerated holes are transported to the NiCo/NF anode to drive hydrazine oxidation. This configuration enables spontaneous (bias-free) hydrogen production, wherein it is spatially and electrochemically coupled to hydrazine oxidation under ambient conditions.[21] Experimentally, the cell successfully produced hydrogen bubbles under illumination, as shown in Fig. 1b. The following sections systematically discuss each technological component contributing to solar-driven hydrogen production.

2.2. NiCo characterization and its HER catalytic performance

The NiCo catalyst was deposited on a Ti foil substrate *via* electrodeposition. The deposition potential was determined based on the linear sweep voltammetry (LSV) curve obtained in NiCo precursor solution, where a single peak was observed and used as the deposition criterion (Fig. S1). Deposition conditions were optimized by evaluating HER activity under varying deposition potentials and durations, with the highest activity achieved at −2.2 V_{RHE} for 600 s (Fig. S2).

X-ray diffraction (XRD) patterns of NiCo exhibited characteristic peaks at 44.2°, 51.5°, and 75.8°, corresponding to the (111), (200), and (220) planes of NiCo (PDF #01-091-1719; Fig. 2a).[13,22] Field-emission scanning electron microscopy (FE-SEM) and energy-dispersive X-ray spectroscopy (EDS) images indicated that Ni and Co were deposited on Ti foil, with O signals attributed to surface natural oxidation (Fig. 2b and c). The Ni/Co composition of the electrodeposited catalyst was quantified using inductively coupled plasma mass spectrometry (ICP-MS) analysis, and the measured Ni/Co ratio was approximately 0.91 (Table S1).

To investigate the synergistic effect between Ni and Co, individual depositions of Ni and Co were conducted under the same conditions as those used for NiCo. As shown in Fig. S3, Ni exhibited a nanosphere morphology, while Co formed a flake-like layer atop the nanospheres. The incorporation of Co significantly influenced morphology, promoting an edge-modified structure that increases the electrochemically active surface area and exposes more active sites.[23]

Electrocatalytic performance was evaluated using LSV measurements in 1.0 M potassium hydroxide (KOH), with a saturated calomel electrode (SCE) as the reference electrode (RE) and a platinum (Pt) electrode as the counter electrode (CE). As shown in Fig. 2d, NiCo exhibited a slightly higher overpotential (η) at η_{10} (191.2 mV) compared to Pt (105.5 mV), but at η_{100}, the overpotential of NiCo (500.1 mV) was comparable to that of Pt (565.9 mV). NiCo required relatively low overpotentials across 10, 50, and 100 mA cm^{-2}, outperforming both Ni and Co. Tafel slope analysis showed that although Pt exhibited the lowest Tafel slope (87.5 mV dec^{-1}), NiCo had a significantly lower slope (122.2 mV dec^{-1}) than Ni (162.9 mV dec^{-1}) and Co (216.9 mV dec^{-1}), indicating improved HER kinetics (Fig. 2e). The Tafel slopes were extracted from the low-overpotential region (<~50 mA cm^{-2}), corresponding to the potential range relevant for photoelectrochemical operation.

Electrochemical impedance spectroscopy (EIS) further validated the superior HER performance of NiCo, showing a low charge transfer resistance (R_{ct}) among the tested catalysts (Fig. 2f and Table S2). Furthermore, NiCo exhibited a larger electrochemical double-layer capacitance (C_{dl}), indicative of an expanded active surface area (Fig. S4). Chronopotentiometry measurements of the NiCo catalyst at 10 mA cm^{-2} demonstrated excellent stability over 9 h in alkaline media (Fig. S5).

Furthermore, we investigated the electronic structure modification in NiCo catalysts *via* X-ray photoelectron spectroscopy (XPS) and X-ray absorption near-edge structure

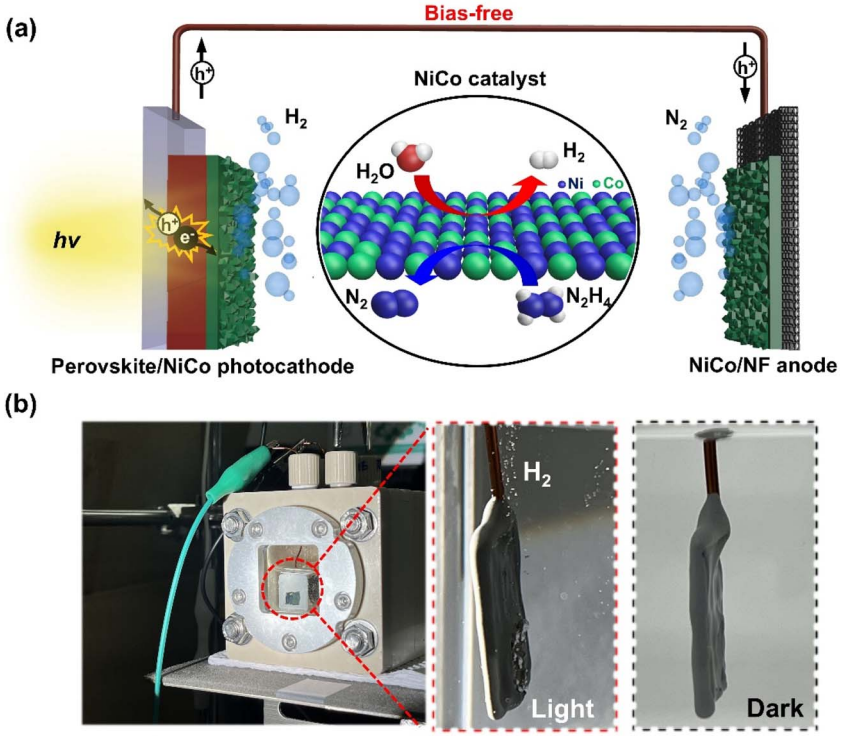

Fig. 1 (a) Schematic illustration of a photoelectrochemical (PEC) cell assembled with a perovskite/NiCo photocathode and NiCo/NF anode for solar hydrogen production. (b) Optical images of an actual unbiased cell and hydrogen bubbles under light and in the dark, evidencing the operational feasibility of the integrated PEC cell.

(XANES). As shown in Fig. 2g and h, the Ni $2p_{3/2}$ spectra of NiCo displayed a negative binding energy shift of 0.2 eV compared to Ni, with distinct peaks assigned to Ni^{2+} at ~855.4 eV and metallic Ni^0 at ~853.6 eV.[24,25] In contrast, the Co $2p_{3/2}$ spectra showed a positive shift of 1.2 eV relative to Co, with Co^{2+} and Co^0 components centered at ~781.2 eV and ~778.4, respectively.[24,25] The opposite binding energy shifts of Ni and Co suggest an intermetallic charge transfer from Co to Ni, effectively increasing the electron density at Ni sites.[25,26] XPS spectra of the O 1s region were also collected for Ni, Co, and NiCo catalysts (Fig. S6).

This interpretation is further supported by Ni and Co K-edge XANES results (Fig. 2i). The absorption edge energy of the Ni K-edge in NiCo appears at a lower energy than that of Ni, indicating partial reduction of Ni. In contrast, the Co K-edge shifts to higher energy compared to Co, consistent with partial oxidation. These results confirm a charge transfer from Co to Ni, reinforcing the XPS-based conclusion of electronic synergy which in turn facilitates water dissociation and contributes positively to water dissociation.[26]

This electronic reconfiguration underpins the Ni–Co synergistic effect, which enhances HER activity by facilitating the water dissociation step considered as a rate-determining step in alkaline electrolyte.[27,28] The oxygen atom of the water molecule preferentially adsorbs onto the Ni^{2+} site. Increased electron density around Ni promotes charge delocalization within the adsorbed H_2O molecule, weakening the O–H bond and facilitating its dissociation. Co modulates the electronic structure of Ni, thereby lowering the activation energy for water dissociation and accelerating HER kinetics.[12]

2.3. HzOR catalytic performance of NiCo

To overcome the high activation energy of the OER, the HzOR was adopted as an alternative anodic reaction due to its significantly lower thermodynamic potential ($E^\circ = -0.33\ V_{RHE}$). As shown in Fig. 3a, when paired with the HER, the overall reaction required only 0.4 V of external bias to achieve 100 mA cm^{-2}, in stark contrast to the 2.1 V required for the conventional HER–OER configuration. This 1.7 V reduction demonstrates the energetic advantage of integrating the HzOR.

A NiCo catalyst was electrodeposited onto Ni foam (NF), forming a three-dimensional, high-surface-area scaffold that is conductive to charge transport and catalytic accessibility. The deposition was optimized at $-2.2\ V_{RHE}$ for 600 s (Fig. S7), ensuring uniform coverage and structural integrity essential for bifunctional operation (Fig. 3b).

The HzOR performance was evaluated in 1.0 M KOH with 0.5 M N_2H_4, compared with Pt, Ni, and Co catalysts (Fig. 3c). Among these, NiCo exhibited the highest current density and the lowest overpotential, indicating superior catalytic activity toward the HzOR. The enhanced HzOR performance likely arises from the same synergistic effects responsible for the improved HER activity. For further insight, the *iR*-corrected LSV curves are presented in Fig. S8, revealing higher current density after compensating for the *iR* drop. To evaluate product

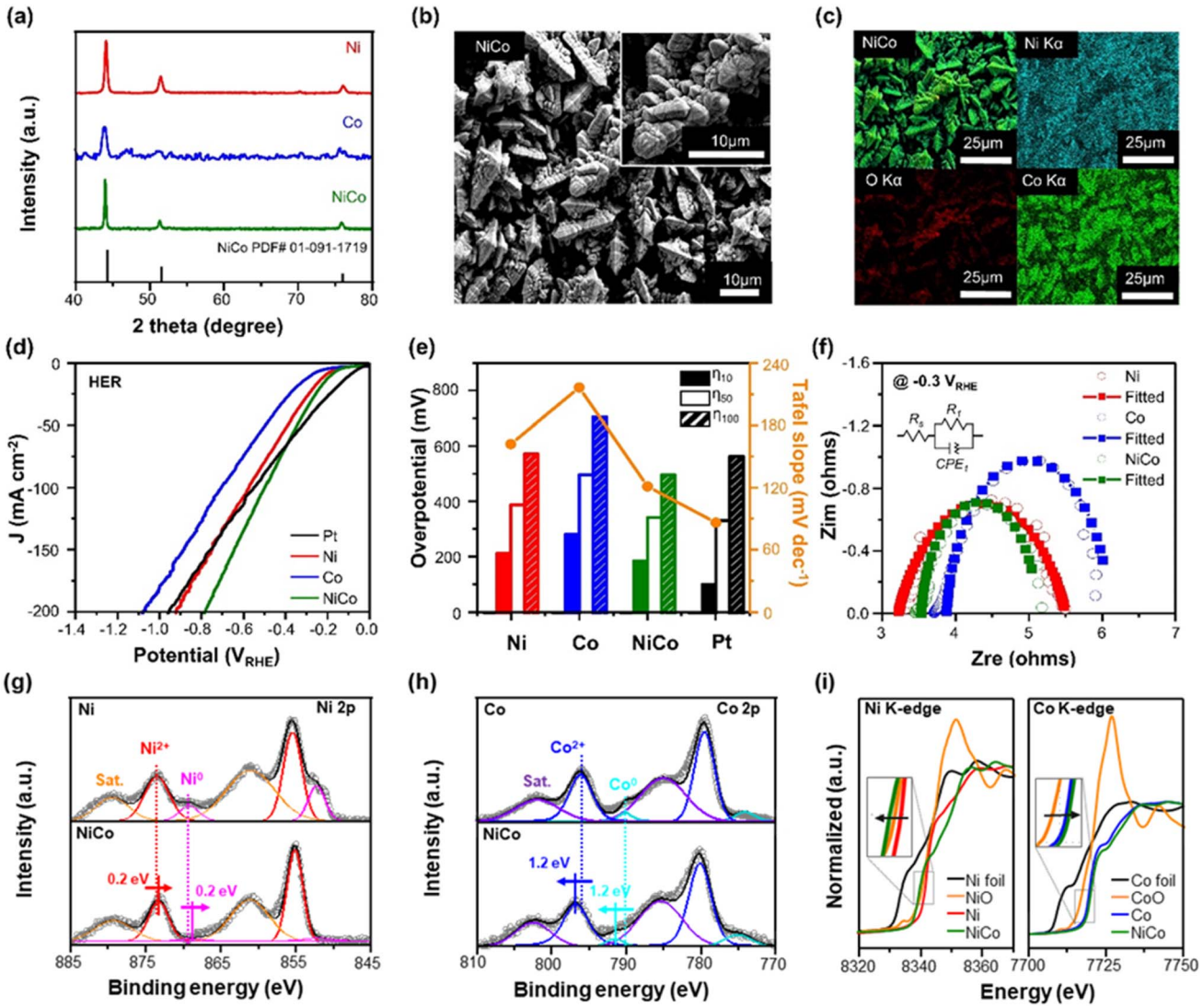

Fig. 2 (a) X-ray diffraction (XRD) patterns of Ni, Co, and NiCo. (b) Field-emission scanning electron microscopy (FE-SEM) images and (c) corresponding energy-dispersive X-ray spectroscopy (EDS) elemental maps of the NiCo catalyst. (d) Linear sweep voltammetry (LSV) curves and (e) the corresponding overpotentials and Tafel slopes of Pt, Ni, Co, and NiCo. (f) Electrochemical impedance spectroscopy (EIS) Nyquist plots at −0.3 V_{RHE}, X-ray photoelectron spectroscopy (XPS) spectra of (g) Ni 2p for Ni and NiCo, and (h) Co 2p spectra for Co and NiCo. (i) Ni and Co K-edge X-ray absorption near-edge structure (XANES) spectra of Ni, Co, NiCo, and reference compounds (Ni foil, NiO, Co foil, and CoO). All electrochemical measurements were performed in 1.0 M KOH.

selectivity, the faradaic efficiency (FE) of N_2 was measured (Fig. 3d). NiCo achieved over 80% FE for N_2, indicating high selectivity of N_2 and minimal side reactions. The remaining minor product was identified as ammonia (NH_3) (Fig. S9 and Table S3). Meanwhile, the faradaic efficiency for hydrogen was 100%.

Additionally, the NiCo catalyst demonstrated comparable current densities and superior HER activity, confirming its role as an effective bifunctional catalyst. Ni showed limited HzOR activity, reinforcing the importance of electronic synergy between Ni and Co in enhancing reaction kinetics (Fig. 3e and Table S4).

A schematic summary of the dual catalytic roles of NiCo is presented in Fig. 3f. Ni sites are primarily responsible for the HER through efficient water reduction. In contrast, Co sites facilitate the HzOR *via* oxidative dehydrogenation of hydrazine. The electronic interaction between Ni and Co enhances charge redistribution and reaction kinetics, enabling a single catalyst to perform both half-reactions efficiently.

The operational durability of the NiCo catalyst under HzOR conditions was validated through 20 consecutive cycles at 20 mA cm^{-2} in alkaline electrolyte containing hydrazine (Fig. 3g). NiCo maintained an FE of 81.6% and N_2 yield rate of 25.4 μmol h^{-1}, demonstrating its durability for long-term operation.

2.4. Perovskite photocathode characterization and its performance

To utilize perovskite solar cells (PSCs) as photocathodes for the HER, we fabricated devices with the architecture ITO/NiO_x/[4-(3,6-dimethyl-9*H*-carbazol-9-yl)butyl]phosphonic acid (Me-

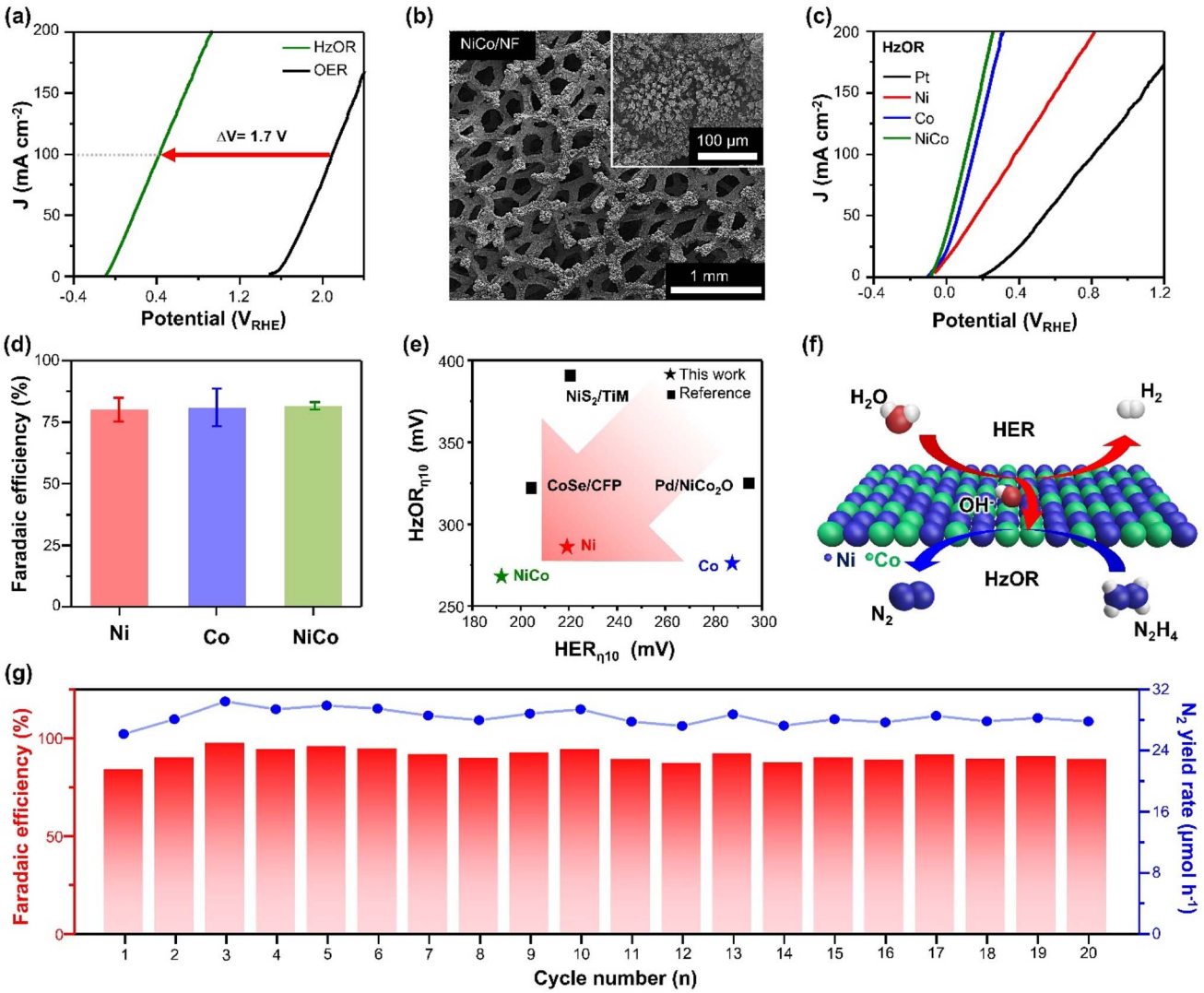

Fig. 3 (a) Comparative LSV curves for the HzOR and OER using NiCo as the anodic catalyst in a three electrode system. (b) FE-SEM images of the NiCo/NF anode with different magnifications. (c) LSV curves and (d) faradaic efficiency for N_2 production using Ni, Co, and NiCo. (e) Comparison of the overpotential for the HER and HzOR with previously reported bifunctional electrocatalysts. (f) Schematic illustration of the bifunctional NiCo catalyst for the HER and HzOR. (g) Cycling stability of NiCo for 20 cycles (1 hour per cycle). The results demonstrate the stability of both faradaic efficiency (%) and the N_2 yield rate (μmol h^{-1}). All electrochemical measurements were performed in 1.0 M KOH containing 0.5 M N_2H_4.

4PACz)/PVK/ETL (electron transport layer)/bathocuproine (BCP)/Ag (Fig. 4a). In this configuration, photogenerated electrons are extracted from the PVK layer, transferred to the top Ag electrode, and ultimately reach the catalyst layer, where the HER occurs. The corresponding cross-sectional SEM image and energy band diagrams are presented in Fig. S10 and 4b, respectively.

In device fabrication, the PVK layer was deposited using a conventional spin-coating method.[29,30] A precursor solution was spin-coated onto the substrate, followed by thermal treatment at 110 °C to form cubic-phase PVK films. Subsequently, FM was deposited on the Ag layer to protect the PVK and facilitate electron transfer to the HER surface. A piece of Ti foil was connected with FM to form a conductive junction, followed by electrodeposition of a NiCo catalyst on Ti foil to complete the photocathode configuration (Fig. S11).[31] Due to the intrinsic moisture susceptibility of PVK materials, the device edges were encapsulated with epoxy resin to prevent water penetration. The stability of these devices was evaluated by immersion tests (Fig. S12).

The optical band gap of PVK was determined from the Tauc plot to be 1.56 eV (Fig. S13a). The resulting films were characterized using SEM and grazing incidence wide-angle X-ray scattering (GIWAXS). SEM images confirmed uniform grain distribution (Fig. S13b), and GIWAXS patterns exhibited diffraction patterns characteristic of the cubic perovskite phase (Fig. S13c).[32–34]

To evaluate the influence of the ETL on photovoltaic performance, we fabricated devices using buckminsterfullerene (C_{60}) and phenyl-C_{61}-butyric acid methyl ester (PCBM), both of which are commonly used in PSCs. Fig. 4c and Table S5 show the current density–voltage (*J*–*V*) characteristics of the devices.

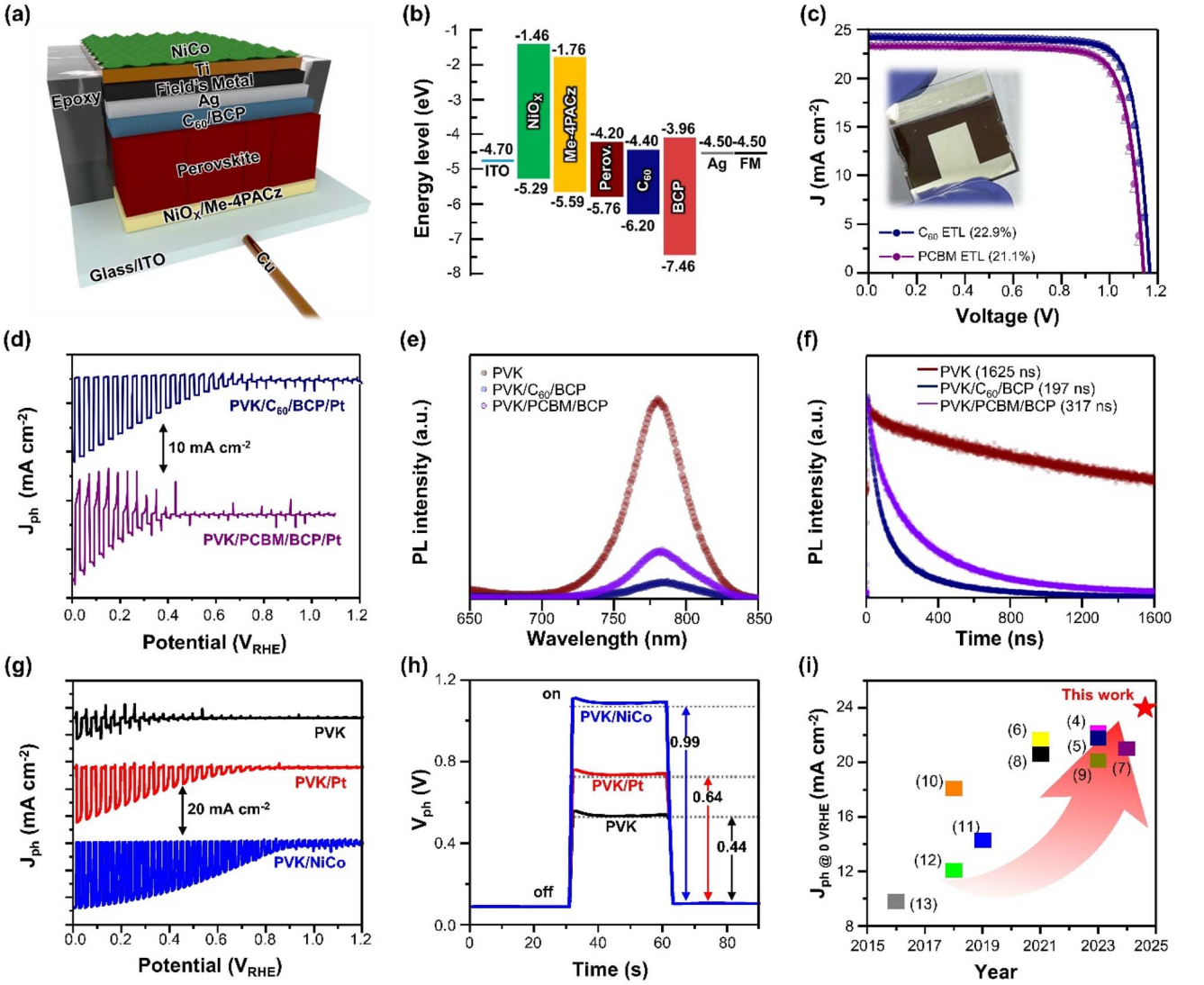

Fig. 4 (a) Schematic illustration and (b) energy band alignment of the PVK/NiCo photocathode. (c) *J*–*V* curves of perovskite solar cells measured in reverse (closed circle) and forward (open triangle) scan directions. (d) LSV curves of the PVK/NiCo photoelectrodes employing different electron transport layers. (e) Steady-state photoluminescence (PL) emission spectra and (f) time-resolved PL spectra with an excitation wavelength of 463 nm for C_{60} and PCBM layers deposited on the PVK layer. (g) LSV curves and (h) open-circuit photovoltage generated by the photocathode under illumination without any externally applied bias. (i) The comparison of the photocurrent density at 0 V_{RHE} with the reported PVK photocathode. The numerical labels correspond to the references listed in Table S7. All PEC measurements were conducted in 1.0 M KOH under simulated 1 sun illumination.

The device employing C_{60} achieved a power conversion efficiency (PCE) of 22.9%, with an open-circuit voltage (V_{OC}) of 1.16 V, a short-circuit current density (J_{SC}) of 24.4 mA cm^{-2}, and a fill factor (FF) of 81.4%. The PCBM-based device showed a PCE of 21.1%, with a V_{OC} of 1.13 V, a J_{SC} of 23.4 mA cm^{-2}, and a fill factor (FF) of 79.8%. The external quantum efficiency (EQE) spectra of the PSCs with each ETL well matched the corresponding values obtained from the *J*–*V* curves (Fig. S13d). The enhanced performance of the C_{60}-based device can be attributed to its higher electron mobility and more favorable energy level alignment with the PVK layer.[35,36]

To investigate how differences in photovoltaic performance influence PEC HER performance, we fabricated devices incorporating a Pt catalyst. Three-electrode measurements were conducted using the perovskite-based device as the working electrode (WE), a saturated calomel electrode (SCE) as the reference electrode, and Pt as the counter electrode (CE), in Ar-saturated 1 M KOH electrolyte under simulated AM 1.5G illumination (100 mW cm^{-2}). As shown in Fig. 4d, the C_{60}-based device exhibited a higher photocurrent density than the PCBM-based device, indicating enhanced PEC HER performance with C_{60} as the ETL. These results demonstrate that enhancing photovoltaic performance can improve the HER performance of PSC-based photocathodes.

To further understand this enhancement, we investigated interfacial charge transfer in devices employing C_{60} and PCBM *via* steady-state photoluminescence (PL) and time-resolved PL (TRPL) measurements. PVK/C_{60} exhibited more effective PL

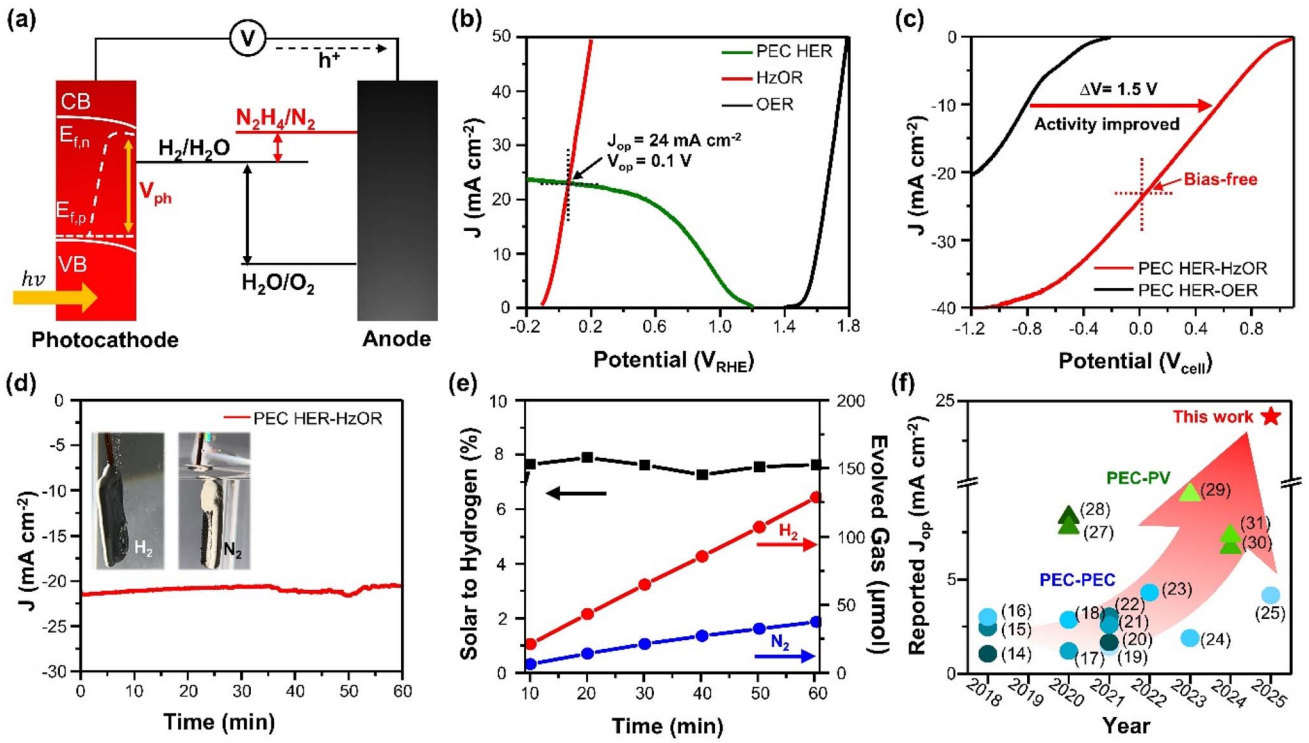

Fig. 5 (a) Schematic illustration of an unbiased two electrode (2E) PEC cell consisting of a PVK/NiCo photocathode and a NiCo/NF anode for simultaneous HER and HzOR. (b) Overlayed LSV curves measured in a 3E configuration for the HER, HzOR and OER. (c) Coupled LSV curves comparing HER–HzOR and HER–OER systems. (d) Chronoamperometry in an unbiased HER–HzOR system. (e) Solar to hydrogen efficiency (left) and quantified evolved gases (right) during unbiased operation under 1 sun illumination. (f) Comparison of the operating photocurrent density (J_{op}) for solar hydrogen production with previously reported systems. The numerical labels correspond to the references listed in Table S8.

quenching compared to the PVK/PCBM sample, indicating more efficient electron transfer in the C_{60}-based devices (Fig. 4e).[35,37] To investigate the charge-extraction dynamics at the PVK/ETL interface, the TRPL decay curves were fitted using a biexponential function. As shown in Fig. 4f and Table S6, the decay time for PVK/C_{60} was 197 ns, which was shorter than that of the PVK/PCBM film (317 ns), further confirming the improved electron extraction capability of C_{60}. Consequently, these results demonstrate that C_{60} enhances charge transfer at the PVK/ETL interface, thereby improving both photovoltaic performance and PEC HER performance.[38,39] Accordingly, the C_{60}-based photocathode was selected for further application in high-performance PEC HER systems.

Building upon the optimized PVK/C_{60}, we evaluated the effect of catalyst integration on PEC activity by comparing bare PVK, Pt-deposited PVK (PVK/Pt), and NiCo-deposited PVK (PVK/NiCo) (Fig. 4g). PVK/Pt served as a benchmark, as Pt nanoparticles are a well-known hydrogen evolution catalyst (HEC). Pt nanoparticles were deposited on the PVK photocathode at −0.1 V_{RHE} for 300 s under illumination, the optimum duration for Pt deposition (Fig. S14). PVK/NiCo delivered a photocurrent density of −24 mA cm^{-2}, exceeding that of PVK/Pt by 1.2 times and that of PVK by 4.0 times. Additionally, NiCo significantly enhanced the photovoltage, as shown by the difference between the open-circuit potential under chopped illumination. PVK/NiCo electrodes showed a positive increase to 0.99 V compared with PVK (0.44 V) and PVK/Pt (0.64 V), indicating improved electron–hole separation (Fig. 4h).

The PVK/NiCo photoelectrode stably produced hydrogen at 0 V_{RHE} for over 6 hours under alkaline conditions, demonstrating the operational durability and chemical robustness of the PVK. This durability suggests that photocorrosion of the PVK material is minimized under both PEC and photovoltaic operating conditions, and that photogenerated charges are effectively transferred to the catalyst without inducing bulk degradation (Fig. S15).

This performance achieved was among the highest reported for perovskite-based photocathodes, validating the effectiveness of NiCo integration and encapsulation strategies in preserving PEC activity (Fig. 4i and Table S7).

2.5. Solar hydrogen production coupled with hydrazine oxidation

To realize fully unbiased hydrogen production, a PEC cell was constructed by coupling a PVK/NiCo photocathode and a NiCo/NF anode. Replacing the OER with the HzOR significantly reduced the anodic overpotential, enabling overall water splitting at lower energy input. This configuration leverages both the high photovoltage of a PVK photocathode and the bifunctional catalytic activity of NiCo (Fig. 5a).

Overlayed LSV curves illustrate that the PVK/NiCo photocathode, when coupled with the HzOR at the NiCo/NF anode,

achieved a current density of 24 mA cm^{-2} at 0.1 V_{RHE} without external bias. This performance substantially outperformed the OER-coupled configuration, which failed to operate under the same condition (Fig. 5b). These results confirm that the HzOR is essential for facilitating efficient hydrogen production in single absorber, unbiased PEC systems.

Experimentally, solar hydrogen production was demonstrated with two electrodes assembled with a PVK/NiCo photocathode and a NiCo/NF anode in 1.0 M KOH containing 0.5 M N_2H_4, as shown in Fig. 5c. The overall reaction started at 1.1 V_{cell} and achieved a photocurrent density of 24 mA cm^{-2} without the need for external bias. The experimentally evaluated solar hydrogen production performance corresponded well to the predictions based on two half-reactions for the PEC HER and HzOR. By compensating the photovoltage from the photocathode under illumination, the solar hydrogen production continued for at least 1 hour under unbiased conditions, exhibiting an STH efficiency of 7.62% (Fig. 5d and e).

Importantly, the PVK/NiCo photocathode retained its PEC HER activity regardless of the presence of hydrazine, demonstrating robustness in both standard and hydrazine-containing electrolytes (Fig. S16). This stability highlights the feasibility of integrating high-performance PVK photocathodes with alternative anodic reactions for cost-effective, energy-efficient hydrogen production. Typically, bias-free PEC cells rely on tandem architectures (photocathode–photoanode or photoelectrode–photovoltaic) to supply sufficient photovoltage for overall water splitting. In contrast, the present system achieves high photocurrent density and a favorable onset potential using a single absorber, thereby eliminating the structural complexity and fabrication challenges of tandem architecture. Achieving such a functional balance in a single absorber PEC cell is particularly demanding, especially considering the inherent instability and catalytic inactivity of most high-performance absorbers under harsh alkaline conditions. In this context, we strictly benchmarked the performance of our single perovskite-based photocathodes within unbiased PEC systems driven by a single photoelectrode under a single light-path condition (Fig. 5f and Table S8). The demonstrated dual functionality of the PVK/NiCo photocathode integrated with the NiCo NF anode—sustained solar hydrogen production and simultaneous hydrazine detoxification—establishes a practical and scalable pathway toward an integrated PEC platform.

3. Conclusion

In this work, we developed a bias-free PEC cell by integrating a PVK photocathode with a bifunctional NiCo electrocatalyst and pairing it with a NiCo/NF anode for the HzOR. Replacing the OER with the HzOR substantially reduced the anodic overpotential, enabling efficient hydrogen production under alkaline conditions without external bias. Our cell achieved the highest photocurrent density of −24 mA cm^{-2} with a photovoltage of 0.99 V under AM 1.5G illumination, achieving stable hydrogen generation without tandem architecture.

The superior performance originates from the dual catalytic activity of NiCo toward both the HER and HzOR, together with Ni–Co electronic synergy that facilitates charge transfer. Importantly, the cell maintained stable, high-current operation in single absorber architecture. Beyond efficient solar-to-hydrogen conversion, the platform simultaneously achieves hydrazine detoxification, providing an environmental co-benefit.

This strategy establishes a generalizable design principle for bias-free PEC cells, demonstrating how alternative anodic reactions and robust electrocatalyst integration can unlock the practical application of single absorber photoelectrodes under kinetically demanding redox conditions.

4. Experimental

4.1. Materials

Ti foil (0.127 mm, 99.94%), a bismuth indium tin ingot (Field's metal, FM), formamidine acetate salt (99%), fullerene (C_{60}), bathocuproine (BCP, sublimed grade, >99.5%), sodium citrate dihydrate ($HOC(COONa)(CH_2COONa)_2 \cdot 2H_2O$), salicylic acid ($C_7H_6O_3$), and sodium hypochlorite (NaOCl) were purchased from Alfa Aesar. Ammonium chloride (NH_4Cl, 99.5%), nickel(II) sulfate hexahydrate ($NiSO_4 \cdot 6H_2O$, 98%), cobalt(II) sulfate heptahydrate ($CoSO_4 \cdot 7H_2O$, 99%), chloroplatinic acid solution (H_2PtCl_6, 8 wt% in water), hydroiodic acid (HI, 57 wt% in water), 2-methoxyethanol (2ME, anhydrous, 99.8%), 2-propanol (IPA, anhydrous, 99.5%), chlorobenzene (CB, anhydrous, 99.8%), *N*,*N*-dimethylformamide (DMF, anhydrous, 99.8%), dimethyl sulfoxide (DMSO, >99.5%), methylammonium chloride (MACl, 98%), sodium hydroxide (NaOH, 97%), nickel(II) nitrate hexahydrate, sodium nitroferricyanide dihydrate ($Na_2[Fe(CN)_5NO] \cdot 2H_2O$), and *p*-dimethylaminobenzaldehyde (*p*-DMAB, 99%) were purchased from Sigma-Aldrich. Sodium sulfate (Na_2SO_4, 99%), ethanol (absolute, 99.9%), and diethyl ether (extra pure grade) were purchased from Duksan. Potassium hydroxide (KOH, 85%) was purchased from Daejung. 2,2′,7,7′-Tetrakis(*N*,*N*-di(4-methoxyphenyl)amino)-9,9′-spirobifluorene (spiro-OMeTAD), and tris(2-(1*H*-pyrazol-1-yl)-4-*tert*-butylpyridine)-cobalt(III) tris(bis(trifluoromethylsulfonyl)imide) (FK209) were purchased from Lumtec. Methylammonium bromide (MABr, >99.99%) was purchased from Greatcell Solar. [4-(3,6-Dimethyl-9*H*-carbazol-9-yl)butyl]phosphonic acid (Me-4PACz), lead(II) iodide (PbI_2, 99.99%), lead(II) bromide ($PbBr_2$, >99.0%), and cesium lead triiodide ($CsPbI_3$, >98%) were purchased from TCI.

4.2. Fabrication of the NiCo electrocatalyst

The NiCo catalyst was synthesized by potentiostatic electrodeposition. Before electrodeposition, the Ti foil substrate was cut into 1 × 1 cm^2 sections and sonicated in acetone, ethanol, and deionized water (DI) for 10 minutes each. The electrodeposition was conducted by applying a constant potential of −2.2 V_{RHE} for 600 s using a three-electrode configuration (3E). The Ti foil served as the working electrode, with a saturated calomel electrode (SCE) as the reference electrode and a platinum electrode as the counter electrode. To prepare the NiCo precursor solution, 1.0 M NH_4Cl, 0.1 M $NiSO_4 \cdot 6H_2O$, 0.1 M $CoSO_4 \cdot 7H_2O$, and 0.4 M H_3BO_3 were dissolved in 80 mL of DI, and experiments were conducted at room temperature. The NiCo deposition on

the Ni foam anode for the hydrazine oxidation reaction (HzOR) was performed using the same method, with only the substrate changed. The Ni foam was cleaned following the same procedure as the Ti foil and electrodeposited under identical conditions. Due to the hazardous nature of hydrazine, it was handled safely by referencing established safety guidelines.[40]

4.3. Fabrication of perovskite solar cells

The perovskite solar cells utilized for the photoelectrochemical hydrogen evolution reaction (PEC HER) in this paper had the architecture ITO/NiO_X/Me-4PACz/perovskite/C_{60} or PCBM/BCP/Ag. The indium tin oxide (ITO, 8 Ω sq^{-1}) substrates were cleaned sequentially by sonication in detergent water, deionized (DI) water, and IPA for 10 min each. NiO_X nanoparticles dispersed in DI water (10 mg mL^{-1}) were spin-coated onto UV–ozone treated ITO substrates at 3000 rpm for 30 s, followed by annealing at 150 °C for 10 min. The NiO_X nanoparticles were synthesized according to a previously reported procedure.[41] For the self-assembled monolayer (SAM) hole transporting layer, Me-4PACz dissolved in ethanol (0.5 mg mL^{-1}) was dropped onto the substrate and spin-coated at 3000 rpm for 30 s, followed by annealing at 100 °C for 10 min. For perovskite layer deposition, the substrate was spin-coated with the perovskite precursor solution at 5000 rpm for 40 s. After spin coating for 10 s, 1 mL of diethyl ether was dropped onto the spinning film. The deposited film was then annealed at 110 °C for 10 min on a hot plate. The perovskite precursor solution was prepared by dissolving 468.9 mg of the synthesized $FAPbI_3$ powder, 11.0 mg of synthesized $MAPbBr_3$ powder, 10.7 mg of CsI, and 9.6 mg of MACl in 0.5 mL DMF/DMSO (9 : 1, v/v). The $FAPbI_3$ and $MAPbBr_3$ powders were synthesized according to a previously reported procedure.[42] Subsequently, thermal evaporation was performed to deposit C_{60} (20 nm), BCP (4.5 nm), and Ag (120 nm) on the perovskite film. When PCBM was used as the ETL, a solution of PCBM (mg mL^{-1} in CB) was spin-coated at 3000 rpm for 30 s.

4.4. Fabrication of the perovskite photocathode

The prepared perovskite solar cell was attached to the silver (Ag) layer using FM for metal encapsulation and heated to 70 °C, melting the FM at its melting point of 62 °C. Once the FM was completely melted, the prepared NiCo catalyst on Ti foil was connected to the FM and cooled to room temperature. Finally, the edges were covered with epoxy resin to ensure perfect encapsulation. For the Pt-deposited perovskite photocathode, the perovskite photocathode was encapsulated without NiCo. The Pt nanoparticles were deposited by photo-assisted electrodeposition the perovskite photocathode at −0.1 V_{RHE} for 300 s in 0.1 M Na_2SO_4 containing 0.5 mM H_2PtCl_6 under simulated 1 sun illumination (AM 1.5G, 100 mW cm^{-2}).

4.5. Characterization

The morphology and elemental mapping of devices were analyzed *via* a scanning electron microscope (FE-SEM, Verios G4 UC, FEI, and Clean-Energy Research Institute, Cryo FIB-SEM, NFEC-2025-03-304629) and energy dispersive spectroscopy (EDS, Hitachi, SU8010) with an accelerating voltage of 15 kV, respectively. X-ray diffraction (XRD, Rigaku, MiniFlex600, Cu Kα radiation, $\lambda = 1.5405$ Å) analysis was performed to investigate the crystal structures of the electrocatalyst. X-ray photoelectron spectroscopy (XPS, Ulvac-phi, PHI700Xi) and a SPECS surface nanoanalysis GmbH, EnviroESCA (Clean-Energy Research Institute, NAP-XPS, NFEC-2025-05-306118) with an electron beam (20 kV, 1 nA) were employed to investigate the oxidation states of the Ni, Co, and NiCo catalysts. All XPS spectra were normalized *via* the C 1s peak to 284.8 eV. Grazing-incidence wide-angle X-ray scattering (GIWAXS) measurements were performed at the 3C beamline of the Pohang Accelerator Laboratory, Republic of Korea. The optical properties of the perovskite film were examined using a UV-vis spectrometer (Shimadzu, UV-2600i). The absorption coefficient (α) of a direct bandgap semiconductor near the band edge can be obtained by using $\alpha h\nu = A(h\nu - E_g)^2$, where A denotes the proportionality constant, $h\nu$ denotes the photon energy, and E_g denotes the optical bandgap. Specifically, E_g was estimated by extrapolating the line tangent to the plotted curve. The steady-state photoluminescence (PL) and time-resolved PL (TRPL) spectra were recorded using a Fluoromax-4 (iHR320, HORIBA Scientific) spectrometer. The excitation wavelength was 463 nm, and the TRPL measurements were performed at the maximum PL (~780 nm) of the perovskite film. Grazing-incidence wide-angle X-ray scattering (GIWAXS) measurements were performed at the 3C beamline of the Pohang Accelerator Laboratory, Republic of Korea.

4.6. Electrochemical measurements for the NiCo catalyst

Linear sweep voltammetry (LSV) curves were measured by scanning the potential range from open-circuit potential (OCP) to −2.0 V_{RHE} at a scan rate of 10 mV s^{-1}. Electrochemical impedance spectroscopy (EIS) was carried out from 1 to 10^5 Hz at −0.3 V_{RHE} with a potential amplitude of 10 mV, and the collected data were fitted using ZMAN 2.5 software. Electrochemical active surface area (ECSA) was estimated by using double layer capacitance (C_{dl}), which was calculated from Δj ($=j_a - j_c$) measured by CV in a non-faradaic window at different scan rates. ECSA can be calculated by using the following eqn (1):

$$\mathrm{ECSA} = \frac{C_{dl}}{C_s} \quad (1)$$

where C_s is the specific capacitance of a smooth planar surface used for ECSA estimation.

4.7. Photoelectrochemical measurements for perovskite solar cells

Under dry conditions (20 ± 5 °C, below 15% RH), the current density–voltage (J–V) curve and MPP tracking characteristics of devices were measured using a Keithley 2400 source under a xenon-lamp-based solar simulator (Newport 91160s, AAA class). A Si solar cell calibrated by the National Renewable Energy Laboratory (NREL) was employed to adjust the light intensity to the AM 1.5G 1 sun condition (100 mW cm^{-2}). The voltage sweep rate was 20 mV with a delay of 20 ms for the reverse (forward) sweeping direction from 1.2 V (−0.1 V) to

−0.1 V (1.2 V). The devices were measured with a SUS304 aperture with an area of 1 cm^2. An IPCE measurement system (PV Measurement, Inc.) was used to characterize incident photon-to-current conversion efficiency (IPCE).

4.8. Photoelectrochemical measurements for the perovskite-based photocathode

The PEC H_2 production was investigated using a three-electrode configuration (3E) consisting of a working photoelectrode (WE), a Pt counter electrode (CE), and a saturated calomel reference electrode (SCE) in 1.0 M KOH under simulated 1 sun illumination. The solar light was provided by a 300 W Xe lamp (Newport, 66984-300XF-R1) with a water filter and an AM 1.5G filter. The light intensity was calibrated against a guaranteed reference from the National Renewable Energy Laboratory (NREL), U.S. Linear sweep voltammetry (LSV) was recorded by sweeping the potential from the open circuit potential (OCP) to 0 V_{RHE} at a scan rate of 10 mV s^{-1} under chopped illumination using a potentiostat (AMETEK, VersaSTAT 3). All potentials measured against the SCE were converted to those against the reversible hydrogen electrode (RHE) using the following eqn (2):

$$E(vs.\ \mathrm{RHE}) = E(vs.\ \mathrm{SCE}) + E(vs.\ \mathrm{SCE})(\mathrm{reference}) + 0.059\ \mathrm{V} \times \mathrm{pH}\ (\mathrm{at}\ 25\ ^\circ\mathrm{C}) \quad (2)$$

where $E(vs.\ \mathrm{SCE})$ (RE, saturated KCl) = 0.241 V *vs.* NHE at 25 °C.

For an unbiased measurement, the PEC cell was filled with 1.0 M KOH containing 0.5 M N_2H_4. Gas products (H_2, N_2 and O_2) were quantified using a gas chromatograph (YL, ChroZen GC) equipped with a thermal conductivity detector (TCD) connected to a Porapak N column and a molecular sieve 13X column utilizing Ar gas as the carrier gas. Before the reaction, the reactor was purged with Ar gas at a flow rate of 15 sccm for 30 minutes to remove residual H_2, N_2 and O_2. The background gas composition was analyzed immediately before the reaction to establish a stable baseline and ensure accurate product quantification.

The faradaic efficiency (FE) for H_2 was determined using the following eqn (3):

$$\mathrm{FE}\ (\eta_F, \%) = [2 \times n\mathrm{H_2}\ (\mathrm{mol}) \times F\ (\mathrm{C\ mol^{-1}})/\mathrm{total\ charge\ passed\ (C)}] \times 100 \quad (3)$$

where $n\mathrm{H_2}$ is the mol of generated H_2 and F is Faraday's constant (96 485.33 C mol^{-1}).

The faradaic efficiency (FE) for N_2 was determined using the following eqn (4):

$$\mathrm{FE}\ (\eta_F, \%) = [4 \times n\mathrm{N_2}\ (\mathrm{mol}) \times F\ (\mathrm{C\ mol^{-1}})/\mathrm{total\ charge\ passed\ (C)}] \times 100 \quad (4)$$

where $n\mathrm{N_2}$ is the mol of generated N_2 and F is Faraday's constant (96 485.33 C mol^{-1}).

The concentrations of hydrazine and ammonia were quantified using UV-vis spectrophotometry at wavelengths of 458 nm (*p*-dimethylaminobenzaldehyde, *p*-DMAB method) and 655 nm (indophenol blue method), respectively. To ensure that the measurements fell within the linear calibration range, electrolyte samples were appropriately diluted with 0.1 M HCl for hydrazine analysis and 1.0 M KOH for ammonia analysis prior to measurement. The concentrations of hydrazine and ammonia were determined based on calibration curves prepared using standard solutions.

The solar-to-hydrogen (STH) conversion efficiency, a critical parameter representing how effectively H_2 is produced by overall water splitting using incident solar energy, was determined using the following eqn (5).[43]

$$\eta_{STH} = [(J_{SC}\ (\mathrm{mA\ cm^{-2}})) \times (0.33\ \mathrm{V}) \times \eta_F/(P_{total}\ (\mathrm{mW\ cm^{-2}}))]_{\mathrm{AM\ 1.5G}} \quad (5)$$

where J_{SC} is the photocurrent density, the value of 0.33 V represents the thermodynamic potential difference between hydrazine oxidation and the hydrogen evolution reaction, η_F is the faradaic efficiency (FE) for H_2 production, and P_{total} is the incident solar power density (100 mW cm^{-2}).

Author contributions

M. L., W. K., and H. K. contributed equally to this work. Y. J. J. and M. J. K. designed and supervised the project. Y. J. J., M. J. K., M. L., W. K., and H. K. designed the concept, analyzed the data, and prepared the manuscript. M. L., W. K., H. K., and S. L. optimized and characterized the photoelectrochemical devices. Y. J. J., M. J. K., M. L., W. K., H. K., and S. L. reviewed and edited the manuscript. All authors discussed the results and commented on the manuscript.

Conflicts of interest

There are no conflicts to declare.

Data availability

The data supporting this article have been included as part of the supplementary information (SI). Supplementary information: experimental details and additional characterization data, including LSV, SEM, ECSA, chronopotentiometry, XPS, UV-vis absorbance, Faradaic efficiency, GIWAXS, EQE, MPPT, ICP-MS, EIS, and TRPL results. See DOI: https://doi.org/10.1039/d5el00192g.

Acknowledgements

This work was supported by the Korea Institute of Energy Technology Evaluation and Planning (KETEP) and the Ministry of Climate, Energy & Environment (MCEE) of the Republic of Korea (RS-2024-00451343) and ERC Center funded by the National Research Foundation of Korea (RS-2022-NR070840). This research was supported by the Basic Science Research Program through the National Research Foundation of Korea (NRF) funded by the Ministry of Education (RS-2025-25400520). This research was supported by Quantum Simulator Development Project for Materials Innovation through the National

Research Foundation of Korea (NRF) funded by the Korean government (Ministry of Science and ICT (MSIT)) (RS-2023-NR119931).

References

1 S. Lee, Y. Lee, H. G. Abbas, S. Ji, S. Y. Kim, K. Lee, S. Li, E. J. Lee, J. Choi and H. Ahn, *Nano Lett.*, 2025, **25**, 7351–7360.
2 M. Lee, J. Kim, J. Kim, Y. J. Jang and J. Y. Kim, *ACS Appl. Electron. Mater.*, 2024, **7**, 331–339.
3 J. Kim, Y. J. Jang, W. Baek, A. R. Lee, J.-Y. Kim, T. Hyeon and J. S. Lee, *ACS Appl. Mater. Interfaces*, 2021, **14**, 603–610.
4 H. Dotan, N. Mathews, T. Hisatomi, M. Grätzel and A. Rothschild, *J. Phys. Chem. Lett.*, 2014, **5**, 3330–3334.
5 J. H. Kim, D. Hansora, P. Sharma, J.-W. Jang and J. S. Lee, *Chem. Soc. Rev.*, 2019, **48**, 1908–1971.
6 Z. Li, S. Fang, H. Sun, R. J. Chung, X. Fang and J. H. He, *Adv. Energy Mater.*, 2023, **13**, 2203019.
7 M. S. Prévot and K. Sivula, *J. Phys. Chem. C*, 2013, **117**, 17879–17893.
8 K. Zhang, M. Ma, P. Li, D. H. Wang and J. H. Park, *Adv. Energy Mater.*, 2016, **6**, 1600602.
9 Y. Luo, Z. Zhang, M. Chhowalla and B. Liu, *Adv. Mater.*, 2022, **34**, 2108133.
10 P. J. Megía, A. J. Vizcaíno, J. A. Calles and A. Carrero, *Energy Fuels*, 2021, **35**, 16403–16415.
11 Z. Y. Yu, Y. Duan, X. Y. Feng, X. Yu, M. R. Gao and S. H. Yu, *Adv. Mater.*, 2021, **33**, 2007100.
12 R. Subbaraman, D. Tripkovic, K.-C. Chang, D. Strmcnik, A. P. Paulikas, P. Hirunsit, M. Chan, J. Greeley, V. Stamenkovic and N. M. Markovic, *Nat. Mater.*, 2012, **11**, 550–557.
13 B. Huner, N. Demir and M. F. Kaya, *ACS Omega*, 2023, **8**, 5958–5974.
14 B. Liu, S. Wang, G. Zhang, Z. Gong, B. Wu, T. Wang and J. Gong, *Chem. Soc. Rev.*, 2023, **52**, 4644–4671.
15 H. Song, S. Luo, H. Huang, B. Deng and J. Ye, *ACS Energy Lett.*, 2022, **7**, 1043–1065.
16 A. K. Jena, A. Kulkarni and T. Miyasaka, *Chem. Rev.*, 2019, **119**, 3036–3103.
17 A. M. Fehr, A. Agrawal, F. Mandani, C. L. Conrad, Q. Jiang, S. Y. Park, O. Alley, B. Li, S. Sidhik and I. Metcalf, *Nat. Commun.*, 2023, **14**, 3797.
18 J. Liu, Y. Du, D. Zheng, S. Wang, Y. Hou, J. Zhang and X. F. Lu, *ACS Mater. Lett.*, 2023, **6**, 466–481.
19 X. M. C. Ta, R. Daiyan, T. K. A. Nguyen, R. Amal, T. Tran-Phu and A. Tricoli, *Adv. Energy Mater.*, 2022, **12**, 2201358.
20 F. Sun, J. Qin, Z. Wang, M. Yu, X. Wu, X. Sun and J. Qiu, *Nat. Commun.*, 2021, **12**, 4182.
21 A. Tayyebi, R. Mehrotra, M. A. Mubarok, J. Kim, M. Zafari, M. Tayebi, D. Oh, S.-h. Lee, J. E. Matthews and S.-W. Lee, *Nat. Catal.*, 2024, **7**, 510–521.
22 D. Gao, J. Guo, H. He, P. Xiao and Y. Zhang, *Chem. Eng. J.*, 2022, **430**, 133110.
23 Z. Wu, Y. Feng, Z. Qin, X. Han, X. Zheng, Y. Deng and W. Hu, *Small*, 2022, **18**, 2106904.
24 R. Zhang, X. Wang, S. Yu, T. Wen, X. Zhu, F. Yang, X. Sun, X. Wang and W. Hu, *Adv. Mater.*, 2017, **29**, 1605502.
25 Q. Zhao, J. Yang, M. Liu, R. Wang, G. Zhang, H. Wang, H. Tang, C. Liu, Z. Mei and H. Chen, *ACS Catal.*, 2018, **8**, 5621–5629.
26 L. Zhu, J. Huang, G. Meng, T. Wu, C. Chen, H. Tian, Y. Chen, F. Kong, Z. Chang and X. Cui, *Nat. Commun.*, 2023, **14**, 1997.
27 Z. Zhu, Y. Lin, P. Fang, M. Wang, M. Zhu, X. Zhang, J. Liu, J. Hu and X. Xu, *Adv. Mater.*, 2024, **36**, 2307035.
28 F. Liu, C. Shi, X. Guo, Z. He, L. Pan, Z. F. Huang, X. Zhang and J. J. Zou, *Adv. Sci.*, 2022, **9**, 2200307.
29 N. J. Jeon, J. H. Noh, Y. C. Kim, W. S. Yang, S. Ryu and S. I. Seok, *Nat. Mater.*, 2014, **13**, 897–903.
30 H. Chen, C. Liu, J. Xu, A. Maxwell, W. Zhou, Y. Yang, Q. Zhou, A. S. Bati, H. Wan and Z. Wang, *Science*, 2024, **384**, 189–193.
31 M. Crespo-Quesada, L. M. Pazos-Outón, J. Warnan, M. F. Kuehnel, R. H. Friend and E. Reisner, *Nat. Commun.*, 2016, **7**, 12555.
32 S. M. Park, M. Wei, J. Xu, H. R. Atapattu, F. T. Eickemeyer, K. Darabi, L. Grater, Y. Yang, C. Liu, S. Teale, B. Chen, H. Chen, T. Wang, L. Zeng, A. Maxwell, Z. Wang, K. R. Rao, Z. Cai, S. M. Zakeeruddin, J. T. Pham, C. M. Risko, A. Amassian, M. G. Kanatzidis, K. R. Graham, M. Grätzel and E. H. Sargent, *Science*, 2023, **381**, 209–215.
33 S. M. Park, M. Wei, N. Lempesis, W. Yu, T. Hossain, L. Agosta, V. Carnevali, H. R. Atapattu, P. Serles, F. T. Eickemeyer, H. Shin, M. Vafaie, D. Choi, K. Darabi, E. D. Jung, Y. Yang, D. B. Kim, S. M. Zakeeruddin, B. Chen, A. Amassian, T. Filleter, M. G. Kanatzidis, K. R. Graham, L. Xiao, U. Rothlisberger, M. Grätzel and E. H. Sargent, *Nature*, 2023, **624**, 289–294.
34 J. Park, J. Kim, H.-S. Yun, M. J. Paik, E. Noh, H. J. Mun, M. G. Kim, T. J. Shin and S. I. Seok, *Nature*, 2023, **616**, 724–730.
35 P. W. Liang, C. C. Chueh, S. T. Williams and A. K. Y. Jen, *Adv. Energy Mater.*, 2015, **5**, 1402321.
36 G. Namkoong, A. A. Mamun and T. T. Ava, *Org. Electron.*, 2018, **56**, 163–169.
37 W. Kim, J. Kim, D. Kim, B. Koo, S. Yu, Y. Li, Y. Kim and M. J. Ko, *npj Flexible Electron.*, 2024, **8**, 20.
38 K. B. Jiang, W. Q. Huang, T. T. Song, P. X. Wu, W. F. Wang, Q. S. Chen, M. S. Wang and G. C. Guo, *Adv. Funct. Mater.*, 2023, **33**, 2304351.
39 L. Wang, W. Lian, B. Liu, H. Lv, Y. Zhang, X. Wu, T. Wang, J. Gong, T. Chen and H. Xu, *Adv. Mater.*, 2022, **34**, 2200723.
40 J. K. Niemeier and D. P. Kjell, *Org. Process Res. Dev.*, 2013, **17**, 1580–1590.
41 J. Humphreys, F. Malagreca, P. Hume, W. Lewis, E. S. Davies, S. P. Argent and D. B. Amabilino, *Dyes Pigm.*, 2022, **197**, 109836.
42 H. Min, M. Kim, S.-U. Lee, H. Kim, G. Kim, K. Choi, J. H. Lee and S. I. Seok, *Science*, 2019, **366**, 749–753.
43 M. G. Walter, E. L. Warren, J. R. McKone, S. W. Boettcher, Q. Mi, E. A. Santori and N. S. Lewis, *Chem. Rev.*, 2010, **110**, 6446–6473.